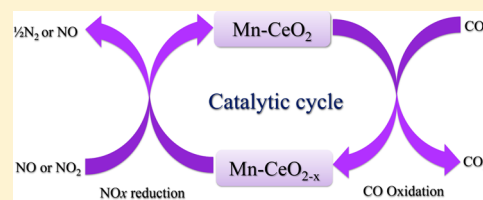


Computational Investigation of CO Adsorption and Oxidation on Mn/CeO₂(111) Surface

Ling-Chieh Hsu,[†] Ming-Kang Tsai,[†] Yu-Huan Lu,[‡] and Hsin-Tsung Chen^{*‡}[†]Department of Chemistry, National Taiwan Normal University, 88, Section 4, Tingchow Road, Taipei 116, Taiwan[‡]Department of Chemistry and Center for Nanotechnology, Chung Yuan Christian University, Chungli 32023, Taiwan

S Supporting Information

ABSTRACT: The interaction and mechanism for CO oxidation on the Mn/CeO₂(111) surface have been studied by using periodic density functional theory calculations corrected with the on-site Coulomb interaction via a Hubbard term (DFT + U). It is found that the Mn dopant facilitates oxygen vacancy formation, while the Mn adatoms may restrain oxygen vacancy formation. In addition, physisorbed CO, physisorbed CO₂, and chemisorbed CO (carbonite, CO₂⁻) species are observed on the Mn-doped CeO₂(111) surface, in contrast, only physisorbed CO is found on the pure CeO₂(111) surface. The vibrational frequency calculations as well as the calculated adsorption energies are carried to characterize these species. The Mn dopant promotes CO oxidation without any activation energy leading to O vacancy formation and CO₂ desorption. The Bader charge analysis is carried to characterize the oxidation state of Mn ions along the catalytic cycle.



1. INTRODUCTION

Ceria (CeO₂) is one of the most efficient catalysts due to its unique oxygen storage properties.¹ However, pure ceria cannot satisfactorily fulfill the elevated activity demands for the CO oxidation catalyst owing to its limited oxygen storage capacity (OSC) and its insufficient thermal stability. Several experimental² and theoretical^{3–5} studies have demonstrated the surface selectivity for the CO oxidation and showed that CO does not adsorb on the stoichiometric CeO₂(111) surface. One of the effective strategies to tackle these problems is to modify ceria with other metal elements. Shapovalov and Metiu⁶ and Camellone and Fabris⁷ showed that the (111) surface of ceria can be made reactive to CO oxidation by doping of the surface with Au theoretically. Yang et al.⁸ also showed the same behavior on the Cu-doped CeO₂(111) surface using the DFT + U methods. Recently, studies of Ti-, Zr-, and Hf-doped CeO₂(110) surfaces reported by Nolan⁹ and La-doped (111) and (110) surfaces reported by Yeriskin and Nolan¹⁰ have shown that the doped surfaces are more reactive to CO adsorption than the undoped ones. The enhancement for CO oxidation by the doping of CeO₂ with other metals have also been evidenced by the experimental investigations.^{11–15}

The manganese–cerium oxides have been extensively identified as a promising and cost-effective catalyst for many important processes, such as oxidation of CO or small hydrocarbon molecules.^{16–20} The reactivity of the modified ceria catalysts is controlled by several factors, such as the size of the metal particle, the pretreatment conditions resulting in different morphology of the catalysts, and the interaction between adding metal and the oxide. As a result, the nature of the active sites on the doping of ceria with other metals and the reaction mechanisms for CO oxidation are still subjects of debate. Higher OSC of Ce_{1-x}Mn_xO₂ ($x = 0.0–0.2$) catalysts

have been synthesized and characterized in the literature.¹⁶ The oxidation state of Mn in the Ce_{1-x}Mn_xO₂ may play a crucial role during the CO oxidation reaction. To the best of our knowledge, no molecular-level study on CO oxidation on Mn/CeO₂ catalysts is available although understanding of the detailed reaction mechanism at the molecular level is very vital for the rational design of novel catalysts for the low temperature CO oxidation.

In the present work, we attempt to address the CO adsorption and the detailed reaction mechanisms of CO oxidation catalyzed by Mn/CeO₂(111). The oxidation states of Mn ions of these catalysts are also characterized. In addition, the step of healing the oxygen vacancies by molecular oxygen is studied to complete a full catalytic cycle for CO oxidation.

The article is organized as follows. The computational details are presented in section 2. The calculated results including the oxygen formation energy of the Mn-doped CeO₂ system, the interaction of Mn adatoms with the stoichiometric CeO₂(111) surface, the adsorption of CO on these surfaces, and the relevant mechanisms for CO oxidation are presented in section 3. A brief summary is given in section 4.

2. COMPUTATIONAL METHODS

Spin-polarized density functional theory (DFT) plane wave calculations were performed by using the Vienna ab initio simulation package (VASP)^{21,22} with the projector augmented wave method (PAW).²³ The electron exchange–correlation functional was treated within the generalized gradient approximation (GGA) with the Perdew–Wang 91 (PW91)

Received: October 22, 2012

Revised: November 29, 2012

Published: December 11, 2012

exchange-correlation functional.^{24–26} The calculations were carried out using the Brillouin zone sampled with $(3 \times 3 \times 3)$ and $(3 \times 3 \times 1)$ Monkhorst-Pack²⁷ mesh k -points grid for bulk and surface calculations, respectively, and with a cutoff energy of 400 eV, which allows to be converged to 0.01 eV in the total energy. Since regular DFT methods have been found unable to describe the localization of the Ce_{4f} states in the reduced ceria,^{28–31} the DFT with the Hubbard U term (DFT + U) method³² was applied to accurately correct the strong on-site Coulomb interactions of Ce_{4f} states.^{28–31,33} Previous studies have showed that there is no general rule on a correct U value to describe the localized $4f$ orbitals of Ce. The proposed U values seem to depend on the oxidation states of Ce and the functional used. For example, Loschen et al.³⁴ proposed a well-balanced U value of 5–6 eV for LDA + U calculations and 2–3 eV for GGA + U calculations. Andersson et al.³⁵ clarified that the U value must satisfy the criteria of $U > 6$ eV for LDA calculations and $U > 5$ eV for GGA calculations to exactly predict the ground state of Ce_2O_x . As such, we chose $U = 6.3$ eV, which has been shown to work well for the metal-doped ceria.^{36–40}

The 12.5% Mn-doped ceria, $Ce_{0.875}Mn_{0.125}O_2$ was modeled by introducing Mn dopants to substitute Ce atoms in the supercell. The reduced systems were created by removing one oxygen atom resulting in an oxygen vacancy concentration of 6.25%. For the surface model, we examined only the (111) surface to characterize the CO– $Ce_{0.875}Mn_{0.125}O_2$ interactions because the (111) surface is energetically the most stable^{41–43} among the low-index $CeO_2(111)$, (110), and (100) surfaces. As shown in Figure 1, the CeO_2 and $Ce_{0.875}Mn_{0.125}O_2(111)$ surface models with 12 atomic layers, a $p(\sqrt{3} \times 2)$ lateral cell, was constructed. In order to examine the effect of Mn cation for CO oxidation, for the $Ce_{0.875}Mn_{0.125}O_2(111)$ surface, one Ce atom of the outermost Ce layer on each side of the $p(\sqrt{3} \times 2)$ $CeO_2(111)$ slab was replaced by an Mn atom. The bottom six layers of the surface model were fixed to the estimated bulk parameters, while the remaining layers were fully optimized. A vacuum space greater than 15 Å was introduced to prevent interactions between slabs. The adsorption energies were calculated by $\Delta E_{ads} = E[\text{surface-adsorbate}] - E[\text{surface}] - E[\text{adsorbate}]$, where $E[\text{surface-adsorbate}]$, $E[\text{surface}]$, and $E[\text{adsorbate}]$ are the calculated electronic energies of adsorbed species on the surface, the bare surface, and the adsorbate in the gas phase, respectively. The climbing image nudged elastic band (CI-NEB) method^{44,45} was applied to map out MEPs after locating plausible local minima. All transition states were verified by the number of imaginary frequencies (NIMG) with NIMG = 1. The charge density difference was carried out using the expression $\Delta\rho_{diff} = \rho[\text{surface + adsorbate}] - \rho[\text{surface}] - \rho[\text{adsorbate}]$, where $\rho[\text{surface + adsorbate}]$, $\rho[\text{surface}]$, and $\rho[\text{adsorbate}]$ are the charge density of adsorbed species on the surface, the bare surface, and the adsorbate, respectively.

3. RESULTS AND DISCUSSION

3.1. Bulk and Surface of Mn-Doped Ceria. To ensure the reliability of the computational results, we first predicted bulk lattice constants and compared them with the experimental values. The geometries of stoichiometric and reduced bulk Mn-doped CeO_2 were optimized at GGA + U levels with considering spin polarization. One should note that the external (cell volume and cell shape) and internal (atomic ions and lattice parameters) degrees of freedom were allowed to relax until forces and stress vanished in the bulk calculations.

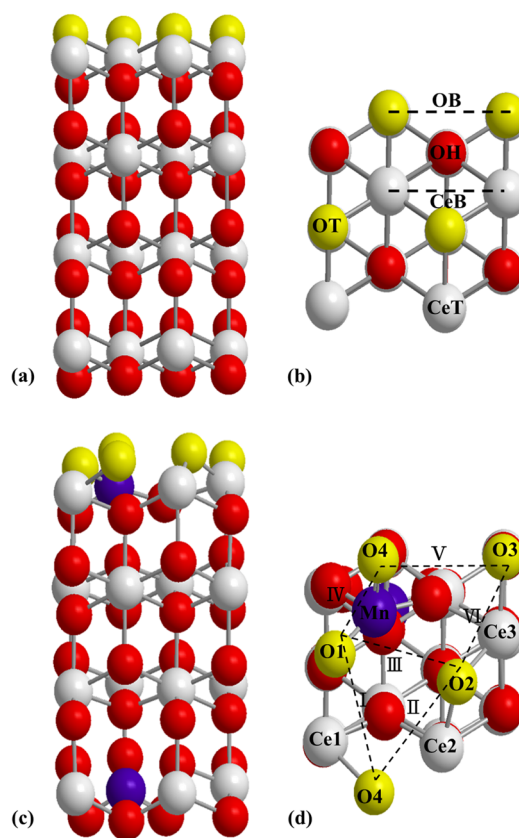


Figure 1. (a) Side view and (b) top view of the $CeO_2(111)$ surface. CeT, CeB, OT, OB, and OH correspond to active sites for Ce top, Ce bridge, O top, O bridge, and O hollow sites, respectively. (c) Side view and (d) top view of the $Ce_{0.875}Mn_{0.125}O_2(111)$ surface model. I, II, III, IV, V, and VI correspond to active sites for O1–O4-long, O2–O4-long, O1–O2-long, O1–O4-short, O3–O4-long, and O2–O3-short sites, respectively. Yellow, red, white, and purple spheres represent the top-layer O, O, Ce, and Mn atoms, respectively. A rectangle represents the supercell used in this work.

The larger cutoff energy and very high-accurate energy were carried to avoid the Pulay stress and related problems. The predicted lattice constant of bulk 12.5% Mn-doped ceria is 5.39 Å, while that for bulk CeO_2 is 5.45 Å. The theoretical values are close to the experimental values of 5.41⁴⁶ and 5.41¹⁶ Å for bulk CeO_2 and Mn-doped ceria. The optimized Ce_8O_{16} unit has all Ce–O bond lengths equal to 2.36 Å, while optimized $Ce_{0.875}Mn_{0.125}O_2$ shows geometric distortions of the oxygen lattice with the longer Ce–O bonds averaging 2.35 Å and the average of shorter Mn–O bonds at 2.22 Å.

The oxygen vacancy formation is described by the reaction of $Ce_{1-x}M_xO_2 \rightarrow Ce_{1-x}M_xO_{2-\delta} + 1/2O_2$.⁴⁷ The oxygen vacancy formation energy, E_f was computed according to eq 1:

$$E_f = E(Ce_{1-x}M_xO_{2-\delta}) + 1/2E(O_2) - E(Ce_{1-x}M_xO_2) \quad (1)$$

where $E(Ce_{1-x}M_xO_2)$ indicates the energy of the bulk or surface $Ce_{1-x}M_xO_2$, $E(O_2)$ is the energy of a gas-phase O_2 , and $E(Ce_{1-x}M_xO_{2-\delta})$ is the energy of the bulk in the presence of one oxygen vacancy. In the present, we only show the formation of oxygen vacancy neighboring the Mn dopant because the required energy for the vacancy further away from Mn dopant is close to the undoped CeO_2 . The calculated E_f of $Ce_{0.875}Mn_{0.125}O_2$ is 0.73 and 0.88 eV depending on the different

Table 1. Lattice Constants and O Vacancy Formation Energy (E_f) of CeO_2 and $\text{Ce}_{0.875}\text{Mn}_{0.125}\text{O}_2$ materials

species	lattice constants		vacancy position	E_f (eV)	
	unreduced	reduced		bulk	surface
CeO_2	5.45(5.41) ^a	5.50		3.27	2.20
$\text{Ce}_{0.875}\text{Mn}_{0.125}\text{O}_2$	5.39	5.45(5.42) ^a	VO1 ^b	0.73, 0.88 ^d	0.58
			VO2		0.71
			VO3		1.89
			VO4		0.64
			$V^*(\text{O}_2)$ ^c		1.29

^aThe values in parentheses are the experimental data. ^bThe labeling of the O atoms is shown in Figure 1d. VO1 means that O1 has been removed and so on. ^cSecond vacancy after VO1. ^dThe different formation energies are calculated from the different coordination shell of the Mn–O bond.

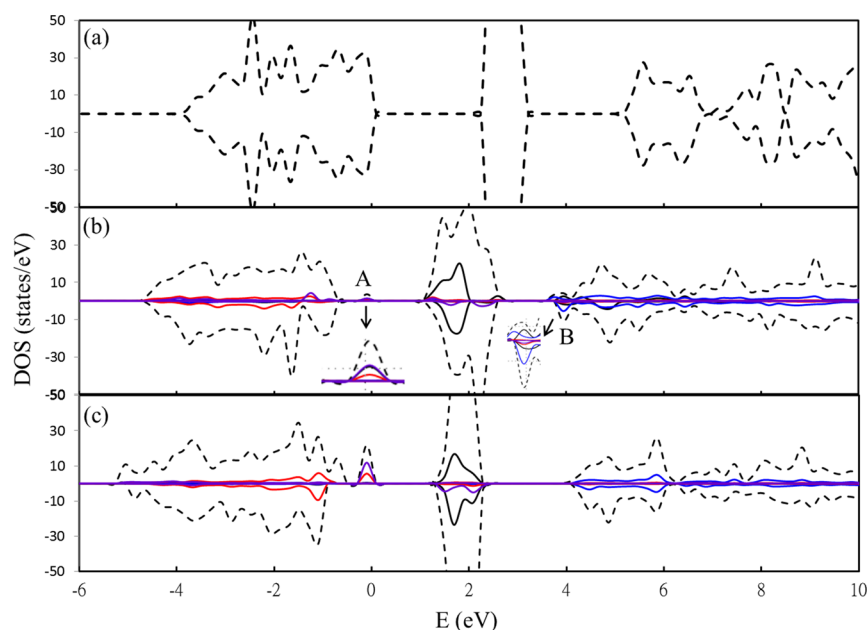


Figure 2. Density of states (DOS) and local density of states (LDOS) for (a) $\text{CeO}_2(111)$ surface, (b) a single Mn atom adsorbed at the hollow site of $\text{CeO}_2(111)$ surface, and (c) $\text{Ce}_{0.875}\text{Mn}_{0.125}\text{O}_2(111)$ surface. The black dashed, black solid, blue, red, and purple lines represent total, Ce(f), Ce(d), O(p), and Mn(d), respectively. The energy at $E = 0$ eV represents the Fermi energy.

coordination shell of the Mn–O bond.³⁶ Compared to CeO_2 and $\text{Ce}_{0.875}\text{M}_{0.125}\text{O}_2$ ($M = \text{Zr}, \text{Fe}, \text{and Ru}$), the smaller E_f (0.73 eV for $\text{Ce}_{0.875}\text{Mn}_{0.125}\text{O}_2$; 3.20 eV for CeO_2 ; and 2.03,³⁷ 1.05,³⁹ and 1.03⁴⁰ eV for $M = \text{Zr}, \text{Fe}, \text{and Ru}$ of $\text{Ce}_{0.875}\text{M}_{0.125}\text{O}_2$) indicates that $\text{Ce}_{0.875}\text{Mn}_{0.125}\text{O}_2$ may show higher OSC property than CeO_2 and other $\text{Ce}_{0.875}\text{M}_{0.125}\text{O}_2$ for $M = \text{Zr}, \text{Fe}, \text{and Ru}$.

The relaxed structure of 12.5% Mn-doped $\text{CeO}_2(111)$ surface in which two Ce atoms are replaced by two Mn atoms is shown in Figure 1c. The predicted surface O vacancy formation energies are shown in Table 1. The formation energies of the various nonequivalent surface oxygen of the top-layer are 0.58, 0.71, 0.64, and 1.89 eV. The nearest neighbor oxygen anions (O1, O2, and O4, see Figure 1d) to Mn cations have much smaller formation energies than that for the undoped $\text{CeO}_2(111)$ surface (2.08 eV) indicating that O vacancy formation is very much facilitated by Mn doping. The formation of a second oxygen vacancy from the O2 site on the optimized surface, with an O vacancy at the O1 site already present (denoted as $V^*(\text{O}_2)$), also needs less energy with an E_f of 1.29 eV. Although it costs more to make the second vacancy than the first one, the vacancy formation energy is still smaller than that of the pure surface. Therefore, the Mn dopant may serve as the seed for the formation of oxygen vacancy clusters on the ceria surfaces.

The stoichiometric $\text{CeO}_2(111)$ system is known to be an insulator, and the features of the electronic density of states (DOS) shown in Figure 2a are well in agreement with previous DFT + U results.⁸ We found that one new feature appears in the band gap, labeled A and B (Figure 2b), which is contributed from the overlap between the Mn(d) states and the O(p) states resulting in the Mn–O binding. Interestingly, no Ce(f) state is found in the band gap indicating that no Ce^{4+} reduces to Ce^{3+} . This is corroborated by the Bader charge calculations, which are carried to characterize the oxidation states in bulk and surface $\text{Ce}_{0.875}\text{Mn}_{0.125}\text{O}_2$. In order to assign the oxidation states of Mn and Ce in the stoichiometric Mn-doped CeO_2 , we did the Bader charge analyses for stoichiometric MnO_2 and CeO_2 ; the calculated Bader charges of Mn and Ce in the stoichiometric MnO_2 (the oxidation state of Mn is +4) and CeO_2 (the oxidation state of Ce is +4) are 4.95 and 9.60 e. The calculated Bader charges of Mn and Ce in stoichiometric bulk and surface $\text{Ce}_{0.875}\text{Mn}_{0.125}\text{O}_2$ are ~ 5.03 e and ~ 9.60 e, which are close to those of MnO_2 (4.95 e) and CeO_2 (9.60 e). Accordingly, in both cases, the oxidation state for Mn and Ce are characterized as +4 and +4. For reduced Ce_2O_3 (the oxidation state of reduced Ce is +3), the calculated Bader charge of reduced Ce is 9.90 e. In reduced $\text{Ce}_{0.875}\text{Mn}_{0.125}\text{O}_{2-\delta}$, the Mn neighboring the O vacancy is still in the +4 oxidation state (the Bader charge is

within 5.05 and 5.07 e), while the Ce⁴⁺ neighboring the O vacancy is reduced to Ce³⁺ (the Bader charge is 9.90 e).

3.2. Mn/CeO₂(111) Surface. Plausible intermediates for the Mn/CeO₂ interactions were initially optimized by placing a single Mn atom at different active sites on the (111) surface, including Ce-top, O-top, Ce–Ce bridge, O–O bridge, and O-hollow, corresponding to CeT, OT, CeB, OB, and OH, respectively, as illustrated in Figure 1b. All optimized structures are presented in Figure S1, Supporting Information. Table 2

Table 2. Adsorption Energies (E_{ads}) of an Mn Adatom on the Stoichiometric CeO₂(111) Surface As Well As on an O and Ce Vacancy and the Calculated Bader Charge of an Mn Atom in These Configurations^a

adsorption site	E_{ads} (eV)	Mn
Ce top	−4.76	5.62 (Mn ²⁺)
Ce bridge	−4.28	5.63 (Mn ²⁺)
O top	−2.35	6.27 (Mn ^{δ+})
O bridge	−4.87	5.73 (Mn ²⁺)
O hollow	−4.89	5.63 (Mn ²⁺)
V _O	−4.19	7.23 (Mn ^{δ−})
O hollow (V _O)	−2.39	5.70 (Mn ²⁺)
V _{Ce}	11.42	5.03 (Mn ⁴⁺)

^aCalculated Bader charges of Mn in MnO and MnO₂ are 5.54 and 4.95 e, respectively.

displays the relative adsorption energies and the calculated Bader charge of Mn atom in these configurations. It is found that the interactions between the Mn atom and the stoichiometric CeO₂(111) surface including charge transfer from the Mn atom to the surface yield the reduction of Ce ions. The Mn adsorbed at the O-hollow site is found to be the most stable adsorption configuration of the Mn/CeO₂(111) system. The predicted adsorption energy and Mn–O distance are

−4.87 eV and 1.96 Å. The Bader charge analysis for the Mn adatom at the O-hollow site reveals that ~1.37 e is transferred from the metal to the oxide resulting in the formation of a positively charged Mn²⁺ cation, see Table 2. The excess charge in the oxide is mostly localized around the surface O atoms bound to Mn and on the three Ce⁴⁺ ions, which reduce to Ce³⁺ (the calculated Bader charge is ~9.90 e). The vacancy formation energy of Mn/CeO₂ system is calculated to be 3.05 eV by removing one of the three equivalent nearest neighbor surface O atoms bound to the Mn atom. This value is larger than that for pure CeO₂(111), suggesting that Mn adsorption on the CeO₂(111) surface may suppress O vacancy formation. A similar behavior is also found at Cu/ and Fe/CeO₂ catalysts.^{8,39}

In addition, the Mn adsorbed at the surface O vacancy site of the partially reduced CeO_{2-x}(111) surface is also studied. The adsorption energy is −2.39 eV, which is less stable than those for an Mn adsorbed on the stoichiometric CeO₂(111) surface indicating that the Mn atom is not likely to occupy an O lattice site. The Bader charge analysis reveals that ~0.23 e is transferred from the oxide to the metal resulting in the formation of a negatively charged Mn^{δ−}. Accordingly, one of two Ce³⁺ is oxidized to Ce⁴⁺ after Mn is adsorbed at the surface O vacancy. The adsorption energy of an Mn adsorbed at the O hollow site on the partially reduced CeO_{2-x}(111) surface is calculated to be −4.19 eV. It turns out that the Mn atom prefers to localize at the O hollow site even on the partially reduced CeO_{2-x}(111) surface. According to the Bader charge analysis, the two excess electrons created by the O vacancy formation give rise to a charge transfer (0.13 e) from the oxide surface to Mn atom, while the remaining 1.87 e are mainly transferred to the three Ce ions in the second atomic layer of the surface. However, the adsorbed Mn atom still remains positively charged in the Mn/CeO_{2-x} system, only except for the Mn adsorbed at the O vacancy (see Table 2).

Table 3. Adsorption Energies (E_{ads}) and Calculated Frequencies of CO on Stoichiometric CeO₂(111), Mn/CeO₂(111), and Ce_{0.875}Mn_{0.125}O₂(111) Surfaces^a

adsorption site	CeO ₂ (eV)	frequency (cm ^{−1})	Ce _{0.875} Mn _{0.125} O ₂ (eV)	frequency (cm ^{−1})	Mn/CeO ₂ (eV)	frequency (cm ^{−1})
physisorption						
Ce1 top	−0.19	2140	−0.29	2161	−0.03	2132
Ce2 top	−0.17	2196	−0.24	2109	−0.11	2121
Ce3 top	−0.17	2124	−0.18	2106	−0.04	2117
O1 top	−0.01	2113			−0.06	2196
O3 top	−0.03	2113			−0.78	2084
O4 top	−0.01	2113	−0.15	2104	−0.81	2104
Mn top					−0.85	2054
O1–O4-long			−0.27	2138		
O2–O4-long			−0.26	2131		
O3–O4-long			−0.34	2128		
O2–O3-short			−0.18	2133		
chemisorption						
Mn top			−2.05	1790		
O–1O2-long			−1.44	1690		
O1–O4-short			−1.91	1765		
CO ₂ formation						
O1 top			−2.84	2388 1315 619		
O2 top			−2.86	2386 1318 632		
O3 top			−2.73	2384 1313 618		

^aThe calculated frequencies are 2136 cm^{−1} for a gas-phase CO and 2377, 1321, and 644 cm^{−1} for a gas-phase CO₂. I, II, III, IV, V, and VI corresponds to active sites for O1–O4-long, O2–O4-long, O1–O2-long, O1–O4-short, O3–O4-long, and O2–O3-short sites, respectively.

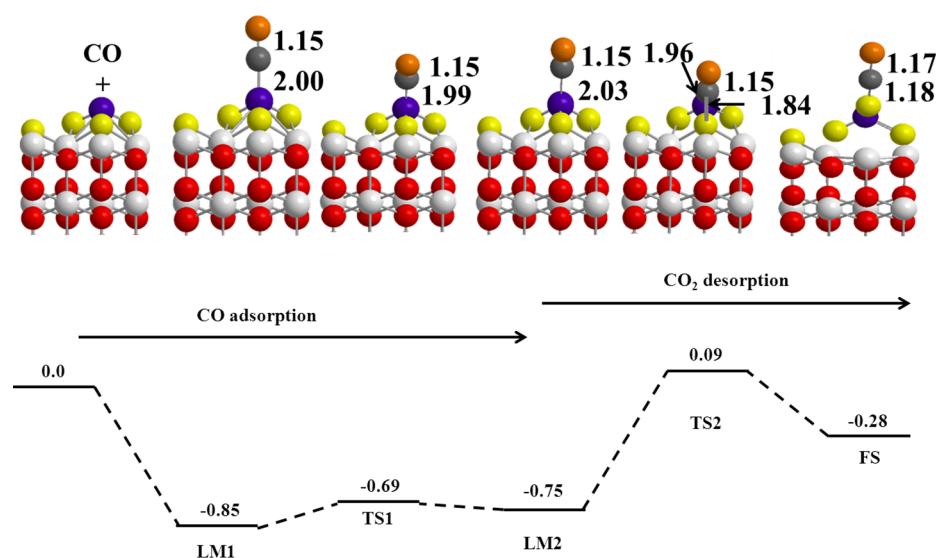


Figure 3. Calculated reaction mechanism and corresponding energies for CO oxidation catalyzed by a supported Mn atom adsorbed at the hollow site of the $\text{CeO}_2(111)$ surface. The relevant bond lengths indicated in the top panels are expressed in angstroms, and the relative energies in the potential energy diagram are expressed in eV.

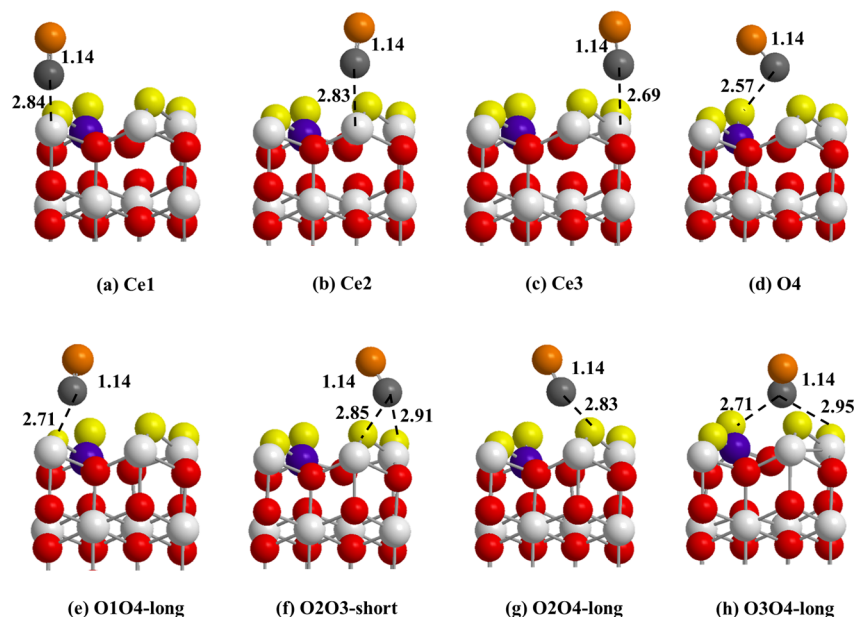


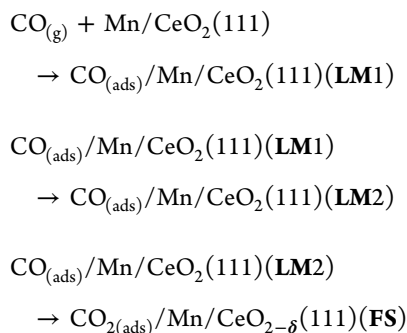
Figure 4. Side view for the optimized structures of CO physisorption on the $\text{Ce}_{0.875}\text{Mn}_{0.125}\text{O}_2(111)$ surface: (a) Ce1, (b) Ce2, (c) Ce3, (d) O4, (e) O1–O4-long, (f) O2–O3-short, (g) O2–O4-long, and (h) O3–O4-long.

3.3. CO Adsorption and Oxidation on Mn-Modified $\text{CeO}_2(111)$ Surfaces. Because of either not binding or binding very weakly for the adsorption O-end toward the surface, we only discuss adsorption with the C-end toward the surface. As shown in Table 3, only weak physisorption of CO on the stoichiometric $\text{CeO}_2(111)$ is found. The result is consistent with the previous studies reported by Huang and Fabris,³ Nolan and Watson,⁴ and Yang et al.⁵ In this study, we explore whether the Mn-modified ceria changes this state of matter. The interactions of a CO molecule with Mn/ $\text{CeO}_2(111)$ and $\text{Ce}_{0.875}\text{Mn}_{0.125}\text{O}_2(111)$ surface were studied.

3.3.1. CO Adsorption and Oxidation on Mn/ $\text{CeO}_2(111)$ Surface. The adsorption of a CO molecule on an Mn adatom in the lowest-energy O hollow site is studied. The predicted structures of CO/Mn/ $\text{CeO}_2(111)$ are shown in Figure S2,

Supporting Information. The CO adsorbed perpendicularly at the Mn adatom is energetically the most stable one among all the calculated structures of CO/Mn/ $\text{CeO}_2(111)$. The calculated adsorption energy and frequency of the C–O are -0.85 eV and 2054 cm^{-1} . The next stable one is found to be the CO tilting adsorbed at the bridge of Mn and O4 adatoms with an adsorption energy of -0.81 eV. The C–O bond lengths of the adsorbed CO molecule are 1.15 and 1.16 Å, essentially unaffected with respect to the calculated value (1.14 Å) of the CO gas-phase; the Mn–C distances are 2.00 and 2.03 Å. However, the CO adsorption on the Mn/ $\text{CeO}_2(111)$ surface becomes stronger than that on the pure $\text{CeO}_2(111)$ surface.

The oxidation of CO catalyzed by Mn/ $\text{CeO}_2(111)$ has been addressed, and the calculated reaction mechanism is illustrated in Figure 3 including the following elementary steps:



First, the CO adsorbs at Mn adatom to form LM1 intermediate with an exothermicity of 0.85 eV. The LM1 isomerizes to LM2 in which the CO tilts from the surface with a slight barrier of 0.16 eV. Then, the adsorbed CO in LM2 oxidizes via a lattice oxygen atom leading to CO₂ desorption and O vacancy formation. This process is the rate-limiting step of the overall reaction with a barrier of 0.84 eV. The overall reaction is slightly exothermic by about 0.28 eV. During the oxidation, the Mn adatom only receives ~0.07 e (the Bader charge of Mn changes from 5.63 to 5.70 e, see Table 2) from the surface and still remains positively charged (Mn²⁺). The formation of a CO₂ from the adsorption of CO at the O hollow site of the Mn/CeO₂(111) surface can be neglected due to requirement of a high barrier of 0.84 eV.

3.3.2. CO Adsorption and Oxidation on Ce_{0.875}Mn_{0.125}O₂(111) Surface. To describe the interactions between a CO molecule and the Ce_{0.875}Mn_{0.125}O₂(111) surface, a CO molecule is placed at the various sites on the Ce_{0.875}Mn_{0.125}O₂(111) surface, including Ce-top, O-top, Mn-top, and O–O bridge, sites, as seen in Figure 1d. Our calculations show that the interactions can divide into three types of adsorption: CO physisorption, CO chemisorption, and CO₂ formation. The optimized configurations of CO physisorption, CO chemisorption, and CO₂ formation are depicted in Figures 4–6, respectively. The calculated adsorption energies of all optimized configurations are shown in Table 3.

CO physisorption is observed at the Ce1, Ce2, Ce3, and O4 top sites as well as at the O-bridge sites (O1–O4-long, O2–O4-long, O3–O4-long, and O2–O3-short). As shown in Table 3, the adsorption energies are between –0.18 and –0.34 eV,

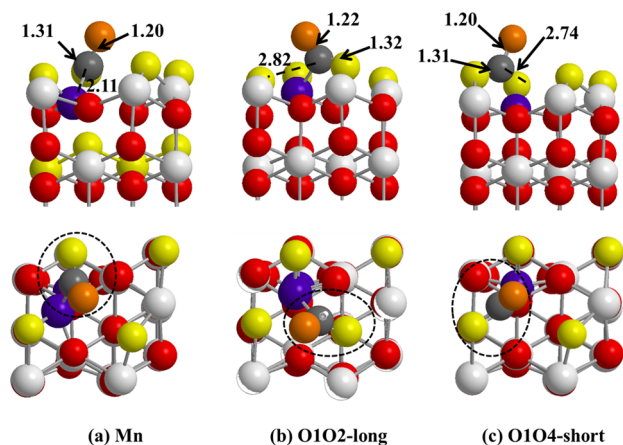


Figure 5. Side view and top view for the optimized structures of CO chemisorption on the Ce_{0.875}Mn_{0.125}O₂(111) surface: (a) Mn, (b) O1–O2-long, and (c) O1–O4-short.

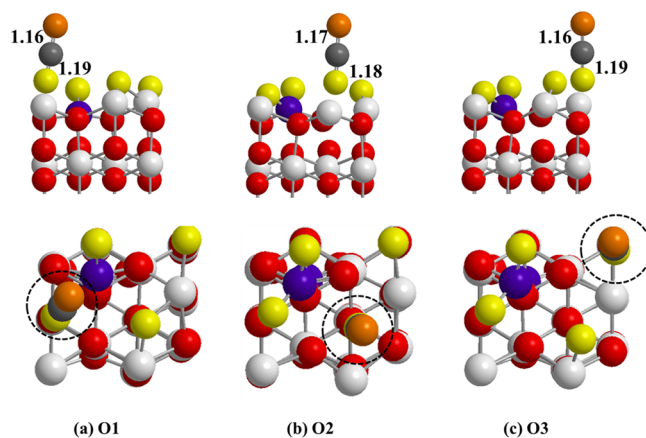


Figure 6. Side view and top view for the optimized structures of CO₂ formation on the Ce_{0.875}Mn_{0.125}O₂(111) surface: (a) O1, (b) O2, and (c) O3.

which is close to those (0.08 and –0.17 eV) for the CO physisorption on the pure CeO₂(111) surface. Different from the CeO₂(111) surface, CO chemisorption is found to occur at the Mn top and the O1–O2-long and O1–O4-short bridge sites. The adsorbed CO binds to one surface oxygen ion forming a carbonite-like species with the CO tilting from the surface. The adsorption energies for the carbonite-like species are –1.91 and –1.44 eV. The C–O and C–O_{surf} bond distances are 1.20–1.22 and 1.31–1.32 Å, which are elongated compared to that of a free CO molecule (1.18 Å). A Bader charge analysis gives net charges of –0.78 to –0.92 e (see Figure 7b,c) for the carbonite-like species and seems to be a

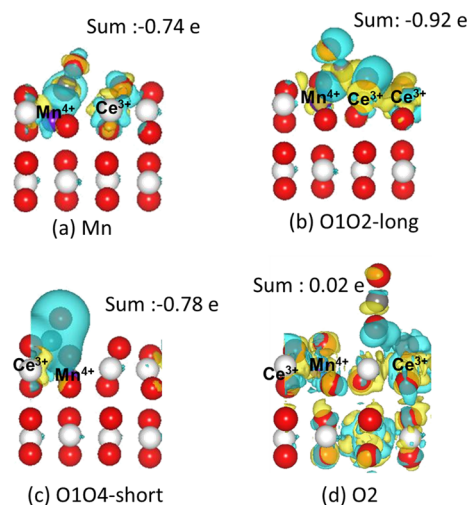


Figure 7. Illustration of charge-density difference for CO oxidation on Ce_{0.875}Mn_{0.125}O₂(111) surface: (a) Mn, (b) O1–O2-long, (c) O1–O4-short, and (d) O2. $\Delta\rho_{\text{diff}}$ isosurfaces were calculated at 0.05 bohr⁻³. The values are effective charges, which are calculated by the Bader analysis program.

reasonable value for a bound CO₂[–] ion. The other CO chemisorption is bound to the surface Mn ions with an adsorption energy of –2.05 eV. The C–O and C–Mn bond distances are 1.20 and 2.11 Å, respectively. A Bader charge analysis gives net charges of –0.74 e (see Figure 7a) for this species indicating a charge transfer from the Mn ion to the CO adsorption. Interestingly, a CO molecule placed at the top of

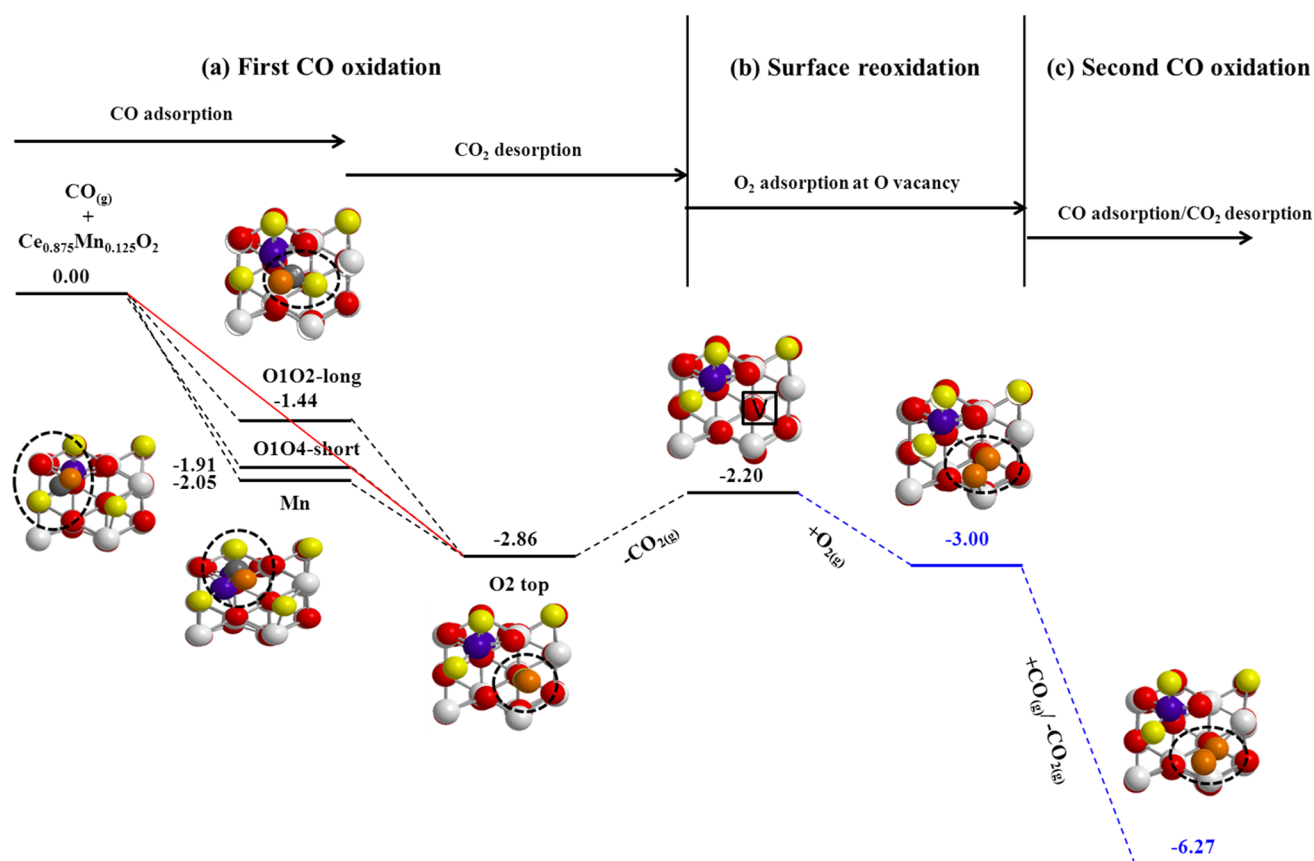


Figure 8. Calculated potential energy diagram for CO oxidation on $\text{Ce}_{0.875}\text{Mn}_{0.125}\text{O}_2(111)$ surface and catalyst regeneration. The proposed catalytic cycle involves (A) the oxidation of a first CO molecule on the stoichiometric $\text{Ce}_{0.875}\text{Mn}_{0.125}\text{O}_2(111)$ surface through participation of a lattice oxygen, leading to O vacancy formation and CO_2 desorption; (B) the adsorption of molecular O_2 at the O vacancy, leading to the formation of surface O adspecies; and (C) the interaction of a CO molecule with these O adspecies, which drives CO oxidation and regeneration of the stoichiometric $\text{Ce}_{0.875}\text{Mn}_{0.125}\text{O}_2(111)$ surface.

surface O1, O2, and O3 ions (see Figure 1d) neighboring the substitutional Mn^{4+} ion leads to the formation of CO_2 floating on the surface with an oxygen vacancy left in the surface. The processes are exothermic and release 2.84, 2.86, and 2.73 eV for a CO at the top of surface O1, O2, and O3, see Table 3. The nature of the adsorbed CO_2 species is similar to a free CO_2 molecule with C–O bond distances close to 1.20 Å and the O–C–O angle of almost 180°. In view of the interactions between the CO_2 molecule and the reduced $\text{Ce}_{0.875}\text{Mn}_{0.125}\text{O}_2(111)$ surface, the CO_2 molecule is weakly bound to the surface with the desorption energies of 0.22–0.37 eV. A Bader charge analysis gives small net charges of 0.02 e (see Figure 7d) for CO_2 species indicating that nearly no charge transfer from the oxide to the CO_2 adsorption results in low adsorption energy (0.22–0.37 eV).

The reaction mechanisms for CO oxidation and catalyst regeneration are depicted in Figure 8 and consist of three steps: (a) $\text{CO}(\text{g}) + \text{Ce}_{0.875}\text{Mn}_{0.125}\text{O}_2(111) \rightarrow \text{CO}_2(\text{g}) + \text{Ce}_{0.875}\text{Mn}_{0.125}\text{O}_{2-\delta}(111)$, the oxidation of a first CO molecule on the stoichiometric $\text{Ce}_{0.875}\text{Mn}_{0.125}\text{O}_2(111)$ surface through participation of a lattice oxygen, leading to O vacancy formation and CO_2 desorption (Figure 8a); (b) $\text{O}_2(\text{g}) + \text{Ce}_{0.875}\text{Mn}_{0.125}\text{O}_{2-\delta}(111) \rightarrow \text{O}/\text{Ce}_{0.875}\text{Mn}_{0.125}\text{O}_2(111)$, the adsorption of molecular O_2 at the O vacancy, leading to the formation of surface O adspecies (Figure 8b); and (c) $\text{CO}(\text{g}) + \text{O}/\text{Ce}_{0.875}\text{Mn}_{0.125}\text{O}_2(111) \rightarrow \text{CO}_2(\text{g}) + \text{Ce}_{0.875}\text{Mn}_{0.125}\text{O}_2(111)$, the interaction of a CO molecule with these O adspecies, which

drives CO oxidation and regeneration of the stoichiometric $\text{Ce}_{0.875}\text{Mn}_{0.125}\text{O}_2$ surface (Figure 8c). Two reaction pathways of the first CO oxidation are considered: the Langmuir–Hinshelwood (LH) and Eley–Rideal (ER) mechanisms as shown in Figure 7. The LH mechanism starts from adsorption of CO with adsorption energies of –1.44, –1.91, and –2.05 eV forming carbonite-like intermediates, which directly produce the adsorption of CO_2 with exothermicities of 1.42, 0.95, and 0.81 eV. The ER mechanism can take place directly by abstracting the surface oxygen ions neighboring the substitutional Mn^{4+} ion and leads to the formation of CO_2 . The process releases –2.86 eV. The desorption of CO_2 with the formation of a surface O vacancy and reducing the neighboring two Ce^{4+} ions to two Ce^{3+} ions requires an energy of 0.66 eV. On the basis of Bader charge population analysis (see Figure 7), we interpret the Mn ion as Mn^{4+} along the most possible mechanism of CO oxidation via the carbonite-like intermediates, while the two neighboring Ce ions reduce to Ce^{3+} ions. The reduced catalysts can be sealed by an O_2 molecule from the gas phase. The adsorption energy of the O_2 molecule on the O vacancy is calculated to be –0.80 eV. The O–O bond length has elongated from the O_2 gas phase value of 1.21 to 1.37 Å, and the Ce^{3+} ion of the surface reoxidized to Ce^{4+} . The O_2 adsorption is assigned to be peroxide according to the predicted vibrational frequency of 794 cm^{-1} .⁴⁸ The resulting O adspecies are active and can promote the direct oxidation of another CO molecule leading to the formation of CO_2 , which desorbs

without any activation barrier and is exothermic by 3.27 eV (see Figure 8c). The Bader charge analysis for the CO oxidation and catalyst regeneration via healing the vacancy by molecular O₂ on the Ce_{0.875}Mn_{0.125}O₂(111) surface shows a catalytic cycle in which the positive oxidation state of the substitutional Mn ion is preserved throughout the reaction.

3.3.3. Vibrational Spectra Calculations. The vibrational frequencies for the adsorbed species, CO molecular, on the Ce_{0.875}Mn_{0.125}O₂(111) surface were predicted as summarized in Table 3. The calculated vibrational frequencies at the region of 2104–2161 cm⁻¹ are attributed to the C–O stretching of CO physisorption in which the values are close to that of a gas-phase CO molecule (2136 cm⁻¹). However, the predicted C–O frequencies of carbonite-like species (1690, 1765, and 1790 cm⁻¹) are in well agreement with the experimental value,^{49,50} 1728 cm⁻¹. The strong red shift of –346 to –446 cm⁻¹ with respect to the gas-phase CO molecule is similar to the observation in experiments for ceria powder with carbonate species and in the theoretical calculations for the CeO₂(110) surface by Yang et al.,⁴⁷ Herschend et al.,⁵¹ and Nolan et al.⁵² Accordingly, the carbonite-like species are assigned to chemisorption. The estimated vibrational frequencies for the antisymmetric stretching mode, symmetric stretching mode, and bending mode of the adsorbed CO₂ species are in the regions of 2384–2388, 1313–1318, and 618–632 cm⁻¹, see Table 3. Compared with the calculated vibrational frequencies of a gas-phase CO₂ (2377, 1321, and 644 cm⁻¹), the frequency shifts of the adsorbed CO₂ species are seen to be very small, indicating and confirming that, indeed, the new adsorption species is likely a weakly adsorbed CO₂ species.

4. CONCLUSIONS

In summary, we provide insight into the interactions of CO with Mn-doped CeO₂(111) surface as well as the catalytic mechanisms for CO oxidation by using periodic DFT + U calculations. Our calculated results show that the Mn dopant facilitates oxygen vacancy formation, while the Mn adatoms may suppress oxygen vacancy formation. Three kind of species, physisorbed CO, physisorbed CO₂ and chemisorbed CO (carbonite, CO₂⁻), are observed on the Mn-doped CeO₂(111) surface; in contrast, only physisorbed CO is found on the clean CeO₂(111) surface. C–O distances, adsorption energies, and C–O vibrational frequencies are used to characterize these species. Incorporating Mn ions into the ceria lattice as substitutional point defects can instead sustain a full catalytic cycle for CO oxidation and catalyst regeneration. The Mn dopant promotes CO oxidation without any activation energy leading to O vacancy formation and CO₂ desorption. Molecular O₂ adsorbs at the O vacancy forming O adspecies that then drive CO oxidation and recover the stoichiometric Mn-doped CeO₂ surface. The Bader charge analysis is carried to character the oxidation state of Mn as +IV ions along the catalytic cycle.

■ ASSOCIATED CONTENT

Supporting Information

Top view and side view of the optimized geometries of adsorbed Mn species at various sites on CeO₂(111) surface. Side view of the optimized geometries of adsorbed CO species at various sites on Mn/CeO₂(111) surface. This material is available free of charge via the Internet at <http://pubs.acs.org>.

■ AUTHOR INFORMATION

Corresponding Author

*E-mail: htchen@cycu.edu.tw.

Notes

The authors declare no competing financial interest.

■ ACKNOWLEDGMENTS

We are grateful to (1) National Science Council, Republic of China, under Grant Numbers NSC 101-2113-M-033-009-MY3 and NSC 101-2632-M-033-001-MY2 and Taiwan National Center for Theoretical Sciences (NCTS) for the financial support and (2) National Center for High-performance Computing, Taiwan, for the computer time and facilities.

■ REFERENCES

- (1) Trovarelli, A. *Catalysis by Ceria and Related Materials*; Imperial College Press: London, U.K., 2002.
- (2) Aneggi, E.; Llorca, J.; Boaro, M.; Trovarelli, A. *J. Catal.* **2005**, *234*, 88.
- (3) Huang, M.; Fabris, S. *J. Phys. Chem. C* **2008**, *112*, 8643.
- (4) Nolan, M.; Watson, G. W. *J. Phys. Chem. B* **2006**, *110*, 16600.
- (5) Yang, Z.; Woo, T. K.; Baudin, M.; Hermansson, K. *J. Chem. Phys.* **2004**, *120*, 7741.
- (6) Shapovalov, V.; Metiu, H. *J. Catal.* **2007**, *245*, 205.
- (7) Camellone, M. F.; Fabris, S. *J. Am. Chem. Soc.* **2009**, *131*, 10473.
- (8) Yang, Z.; He, B.; Lu, Z.; Hermansson, K. *J. Phys. Chem. C* **2010**, *114*, 4486.
- (9) Nolan, M. *J. Phys. Chem. C* **2009**, *113*, 2425.
- (10) Yeriskin, I.; Nolan, M. *J. Chem. Phys.* **2009**, *131*, 244702.
- (11) Bueno-Lopez, A.; Krishna, K.; Makkee, M.; Moulijn, J. A. *Catal. Today* **2007**, *121*, 237.
- (12) Fierro-Gonzales, J. C.; Gates, B. C. *Catal. Today* **2007**, *122*, 201.
- (13) Hernández, W. Y.; Centeno, M. A.; Romero-Sarria, F.; Odriozola, J. A. *J. Phys. Chem. C* **2009**, *113*, 5629.
- (14) Patil, S.; Seal, S.; Guo, Y.; Schulte, A.; Norwood, J. *Appl. Phys. Lett.* **2006**, *88*, 243110.
- (15) Wang, X.; Rodriguez, J. A.; Hanson, J. C.; Gamarra, D.; Martinez-Arias, A.; Fernandez-Garcia, M. *J. Phys. Chem. B* **2005**, *109*, 19595.
- (16) Murugan, B.; Ramaswamy, A. V.; Srinivas, D.; Gopinath, C. S.; Ramaswamy, V. *Chem. Mater.* **2005**, *17*, 3983.
- (17) Pérez-Omil, J. A.; Delgado, J. J.; Ouahbi, W.; Hungria, A. B.; Browning, N.; A. Cauqui, M.; Rodríguez-Izquierdo, J. M.; Calvino, J. J. *J. Phys. Chem. C* **2010**, *114*, 8981.
- (18) Shi, L.; Chu, W.; Qu, F.; Luo, S. *Catal. Lett.* **2007**, *113*, 59.
- (19) Tang, X.; Li, Y.; Huang, X.; Xu, Y.; Zhu, H.; Wang, J.; Shen, W. *Appl. Catal., B* **2006**, *62*, 265.
- (20) Zhou, G.; Shah, P.; Gorte, R. *Catal. Lett.* **2008**, *120*, 191.
- (21) Kresse, G.; Hafner, J. *Phys. Rev. B* **1993**, *47*, 558.
- (22) Kresse, G.; Furthmüller, J. *Phys. Rev. B* **1996**, *54*, 11169.
- (23) Blöchl, P. E. *Phys. Rev. B* **1994**, *50*, 17953.
- (24) Perdew, J. P.; Burke, K.; Ernzerhof, M. *Phys. Rev. Lett.* **1996**, *77*, 3865.
- (25) Perdew, J. P.; Chevary, J. A.; Vosko, S. H.; Jackson, K. A.; Pederson, M. R.; Singh, D. J.; Fiolhais, C. *Phys. Rev. B* **1992**, *46*, 6671.
- (26) Perdew, J. P.; Wang, Y. *Phys. Rev. B* **1992**, *45*, 13244.
- (27) Monkhorst, H. J.; Pack, J. D. *Phys. Rev. B* **1976**, *13*, 5188.
- (28) Nolan, M.; Grigoleit, S.; Sayle, D. C.; Parker, S. C.; Watson, G. W. *Surf. Sci.* **2005**, *576*, 217.
- (29) Nolan, M.; Parker, S. C.; Watson, G. W. *Surf. Sci.* **2005**, *595*, 223.
- (30) Fabris, S.; de Gironcoli, S.; Baroni, S.; Vicario, G.; Balducci, G. *Phys. Rev. B* **2005**, *71*, 041102.
- (31) Fabris, S.; Vicario, G.; Balducci, G.; de Gironcoli, S.; Baroni, S. *J. Phys. Chem. B* **2005**, *109*, 22860.
- (32) Dudarev, S. L.; Botton, G. A.; Savrasov, S. Y.; Humphreys, C. J.; Sutton, A. P. *Phys. Rev. B* **1998**, *57*, 1505.

- (33) Chen, H.-T.; Choi, Y. M.; Liu, M.; Lin, M. C. *ChemPhysChem* **2007**, *8*, 849.
- (34) Loschen, C.; Carrasco, J.; Neyman, K. M.; Illas, F. *Phys. Rev. B* **2007**, *75*, 035115.
- (35) Andersson, D. A.; Simak, S. I.; Johansson, B.; Abrikosov, I. A.; Skorodumova, N. V. *Phys. Rev. B* **2007**, *75*, 035109.
- (36) Chen, H.-L.; Chang, J.-C.; Chen, H.-T. *Chem. Phys. Lett.* **2011**, *502*, 169.
- (37) Chen, H.-T.; Chang, J.-C. *J. Chem. Phys.* **2010**, *132*, 214702.
- (38) Jiang, Y.; Adams, J. B.; Schilfgaarde, M. V. *J. Chem. Phys.* **2005**, *123*, 064701.
- (39) Chen, H.-T.; Chang, J.-C. *J. Phys. Chem. C* **2011**, *115*, 14745.
- (40) Chen, H.-T. *J. Phys. Chem. C* **2012**, *116*, 6239–6246.
- (41) Yang, Z. X.; Woo, T. K.; Baudin, M.; Hermansson, K. *J. Chem. Phys.* **2004**, *120*, 7741.
- (42) Lyons, D. M.; Ryan, K. M.; Morris, M. A. *J. Mater. Chem.* **2002**, *12*, 1207.
- (43) Lyons, D. M.; McGrath, J. P.; Morris, M. A. *J. Phys. Chem. B* **2003**, *107*, 4607.
- (44) Mills, G.; Jönsson, H.; Schenter, G. *Surf. Sci.* **1995**, *324*, 305.
- (45) Henkelman, G.; Uberuaga, B. P.; Jönsson, H. *J. Chem. Phys.* **2000**, *113*, 9901.
- (46) Kummerle, E. A.; Heger, G. *J. Solid State Chem.* **1999**, *147*, 485.
- (47) Yang, Z.; Woo, T. K.; Hermansson, K. *Chem. Phys. Lett.* **2004**, *396*, 384.
- (48) Chen, H.-T.; Chang, J.-C.; Chen, H.-L.; Ju, S.-P. *J. Comput. Chem.* **2009**, *30*, 2433.
- (49) Li, C.; Sakata, Y.; Arai, T.; Domen, K.; Maruya, K.; Onishi, T. *J. Chem. Soc., Faraday Trans 1* **1989**, *85*, 929.
- (50) Li, C.; Sakata, Y.; Arai, T.; Domen, K.; Maruya, K.; Onishi, T. *J. Chem. Soc., Faraday Trans 1* **1989**, *85*, 1451.
- (51) Herschend, B.; Baudin, M.; Hermansson, K. *Chem. Phys.* **2005**, *328*, 345.
- (52) Nolan, M.; Parker, S. C.; Watson, G. W. *Surf. Sci.* **2006**, *600*, 175.